Biosensors and Bioelectronics 212 (2022) 114389

Contents lists available at ScienceDirect

Biosensors and Bioelectronics

journal homepage: www.elsevier.com/locate/bios

Construction of a magnetic-fluorescent-plasmonic nanosensor for the determination of MMP-2 activity based on SERS-fluorescence dual-mode signals

Lin Liu [a], Hongyu Chu [b], Jukun Yang [a], Ying Sun [a], Pinyi Ma [a,**], Daqian Song [a,*]

[a] College of Chemistry, Jilin Province Research Center for Engineering and Technology of Spectral Analytical Instruments, Jilin University, Qianjin Street 2699, Changchun, 130012, China

[b] Nanomedicine Translational Research Center, China-Japan Union Hospital of Jilin University, Sendai Street 126, Changchun, 130033, China

ARTICLE INFO

Keywords:
Matrix metalloproteinase 2
Magnetic-fluorescent-plasmonic nanosensor
Surface-enhanced Raman spectroscopy
Fluorescence
Dual-mode assay

ABSTRACT

Matrix metalloproteinase 2 (MMP-2) is a crucial biomarker of tumor growth, invasion and metastasis. In the present study, a core-satellite magnetic-fluorescent-plasmonic nanosensor (FMNS@Au) was constructed through biological self-assembly to generate localized SERS "hot spots" and an efficient FRET system for the sensitive determination of MMP-2 activity in a SERS-fluorescence dual-mode assay. In this hybrid nanosensor, a biotin-labeled peptide containing a specific MMP-2 substrate (PLGVR) was employed as a bridge for the assembly of gold nanoparticles (AuNPs) and avidin functionalized fluorescent-magnetic nanospheres (FMNS). The modified RB on FMNS served as a Raman reporter and a donor of FRET, while the AuNPs assembled on FMNS acted as SERS substrates and acceptors of FRET. In the presence of MMP-2, the SERS "hot spot" effect was weakened and the FRET system was disrupted through enzymatic cleavage of PLGVR, resulting in a reduction of SERS signal and the recovery of fluorescence emission. Importantly, this combination of SERS and fluorescence assay methods in the dual-mode nanosensor broadened the detection range for MMP-2 to 1–200 ng mL^{-1}, with a limit of detection of 0.35 ng mL^{-1} and a limit of quantitation of 1.17 ng mL^{-1}. In addition, our novel nanosensor affords semi-quantitative sensing of MMP-2 by naked-eye observation and accurate detection of MMP-2 through dual-mode analysis. The practicality of FMNS@Au was validated by determination of MMP-2 activity in cell secretions and human serum samples. The designed FMNS@Au nanosensor holds great potential for clinical diagnosis of protease-related diseases.

1. Introduction

Matrix metalloproteinases (MMPs), a family of extracellular Zn^{2+}-dependent endopeptidases, degrade extracellular matrix (ECM) proteins and important components of the basement membrane, and play essential roles in tumor invasion and metastasis (Kessenbrock et al., 2010; Lei et al., 2020; Quintero-Fabian et al., 2019; Li et al., 2014). Indeed, elevated MMP activity levels are closely associated with invasiveness, angiogenesis, and metastasis, three important characteristics of cancer progression. Among of the MMPs, MMP-2 acts as a potential biomarker and it is overexpressed in the majority of solid tumors, including breast, osteosarcoma, prostate, hepatoma and colon cancers (Davies et al., 1993; Fang et al., 2000; Sheen-Chen et al., 2001; Stearns and Wang, 1993). Hence, the accurate and rapid measurement of MMP-2 secretion activity is of great significance for the clinical diagnosis and prognosis of cancers.

To date, a series of analytical assays, including colorimetric methods, fluorescence methods, electrochemical methods, zymography methods and surface enhanced Raman spectroscopy (SERS) methods have been reported for the determination of MMP-2 activity with high sensitivity (Cheng et al., 2017; Li et al., 2020; Lin et al., 2021; Puperi et al., 2016; Xi et al., 2020). Wang et al. reported the development of a fluorescence resonance energy transfer (FRET) nanosensor for the determination of MMP-2, and this was constructed by connecting upconversion nanoparticles and carbon nanoparticles with a polypeptide that contains a specific MMP-2 substrate (PLGVR) (Wang et al., 2012). Yang et al.

* Corresponding author.
** Corresponding authors.
E-mail addresses: mapinyi@jlu.edu.cn (P. Ma), songdq@jlu.edu.cn (D. Song).

https://doi.org/10.1016/j.bios.2022.114389
Received 31 March 2022; Received in revised form 9 May 2022; Accepted 15 May 2022
Available online 20 May 2022

reported the use of multi-armed horse radish peroxidase (HRP)-labeled graphene oxide for ultrasensitive electrochemical analysis of MMP-2 (Yang et al., 2013). Gong et al. proposed a class of optical interference-free surface enhanced Raman spectroscopy (SERS) nanotags (CO-nanotags) for the multiplex sensing of different MMPs (Gong et al., 2017). However, most of the above assays employed a single testing technique, and are only capable of detecting MMP-2 activity in single mode, greatly narrowing the scope of their practical application in cancer diagnosis.

Nowadays, dual-mode sensing platforms have attracted a great deal of attentions, and this strategy has been demonstrated to be more efficient than the single-mode strategy (Li et al., 2018). A number of dual-mode assays have been proposed, including ICP-MS/fluorescence and fluorescence/colorimetric dual-mode methods, photoacoustic/magnetic resonance imaging and fluorescence/SERS dual-mode sensing (Cao et al., 2015; Liu et al., 2017; Yan et al., 2019; Huang et al., 2019; Gao et al., 2019). Among these strategies, the fluorescence/SERS dual-mode detection platform has been demonstrated to be an exceedingly reliable analytical tool in biosensing fields. Furthermore, fluorescence/SERS dual-mode sensing platforms can be used to visualize analytes simply with the naked eye, and to provide precise quantitative results from the SERS analysis in convenient and rapid features (Li et al., 2021; Sun et al., 2020; Zhang et al. 2019, 2021).

To achieve the full potential of the fluorescence/SERS dual-mode strategy, multifunctional nanomaterials that can be used for SERS and fluorescence dual-mode detection are required. More recently, plasmonic nanoparticles, especially gold nanoparticles (AuNPs), have drawn intense attention in this regard, and they are generally considered to be excellent candidates for the preparation of SERS substrates and fluorescence quenchers (Krpetic et al., 2012; Yang et al., 2015). However, highly sensitive SERS detection with individual AuNPs has proved difficult to realize. To address this problem, the assemblies of hybrid nanosensors may be used to magnify the SERS signals and to establish FRET systems. Currently, magnetic nanoparticles (MNPs) are used as smart probes in biosensing fields because of their superior separation and enrichment capabilities, two qualities which are beneficial for the enhancement of detection efficiency and sensitivity (Farka et al., 2017; Wang et al., 2015). In fluorescence/SERS dual-mode platforms, the application of assemblies of AuNPs and MNPs may be an ideal strategy to increase the distribution of "hot spots" for amplification of SERS signals.

With these considerations in mind, we have designed and constructed (by biological self-assembly) a core-satellite magnetic-fluorescent-plasmonic multifunctional nanosensor (termed as FMNS@Au) with intensified SERS "hot spots" and an efficient FRET system for the sensitive and convenient detection of MMP-2 activity. Fabrication of this novel FMNS@Au dual-mode nanosensor and its underlying sensing principle are both illustrated in Scheme 1. First, fluorescent-magnetic

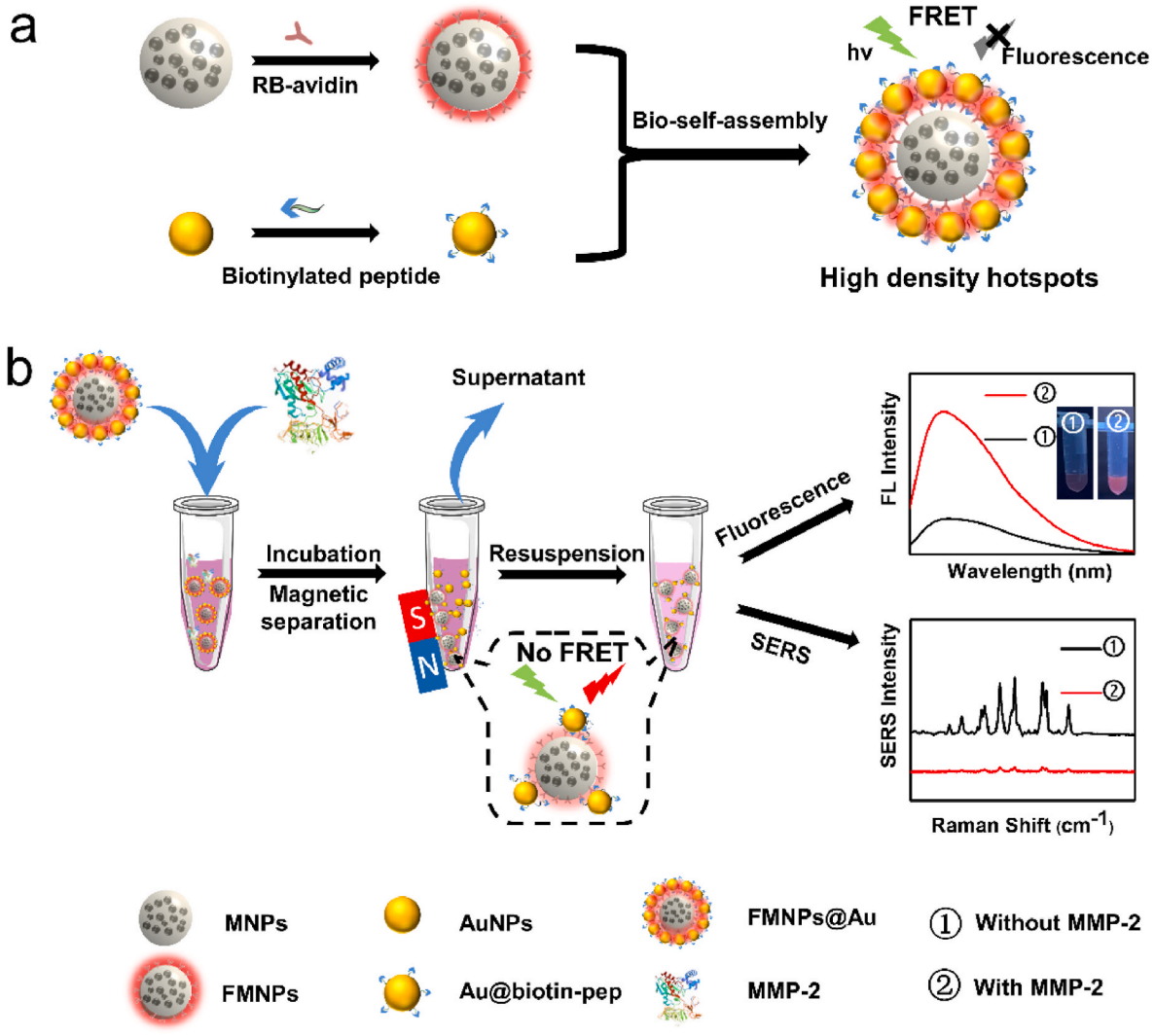

Scheme 1. (a) Schematic fabrication process for the FMNS@Au nanosensor. (b) Sensing principle of the FMNS@Au dual-mode nanosensor for MMP-2.

nanospheres (FMNS) were constructed by covalently connecting RB-avidin (Rhodamine B modified avidin) with magnetic polystyrene nanospheres (MNS). Next, a biotin labeled peptide containing a specific recognition substrate (PLGVR) for active MMP-2 cleavage was used to assemble AuNPs onto the surface of FMNS through specific biological recognition between avidin and biotin.

In this hybrid nanosensor, the assembled AuNPs have a dual function. Thus, the AuNPs act as a FRET acceptor, quenching RB fluorescence emission, and as a nucleus for the formation of SERS "hot spots", ensuring the sensitive determination of MMP-2 activity. The RB is utilized as a donor in the FRET system, and as a Raman reporter. After specific MMP-2 cleavage of the nanosensor peptide, AuNPs are released from the nanosensor and removed by magnetic separation. As a result, the SERS "hot spot" effect is reduced and the FRET system is disrupted, weakening the SERS signal from RB and re-establishing its fluorescence signal. Thus, our novel hybrid nanosensor combines the advantages of high sensitivity of SERS and intuitive visualization of fluorescence. Importantly, precise monitoring of MMP-2 activities in cell secretions and human serum samples could be achieved by using our novel assembled dual-mode nanosensor.

2. Experimental section

2.1. Fabrication of FMNS@Au through biological molecular self-assembly

The self-assembly of the scheming FMNS@Au was accomplished through the highly specific biological recognition between avidin and biotin. Here, 1 mL of 3 nmol L^{-1} biotin-pep modified AuNPs was added to 900 μL of 2 mg mL^{-1} FMNS solution. The mixture was then oscillated on a vortex mixer at room temperature for 8 h. The resulting FMNS@Au nanosensors were then isolated by a magnetic scaffold and washed three times with PBS to remove excess biotin-pep modified AuNPs. Finally, the resulting FMNS@Au nanosensors were resuspended in deionized water for further use.

2.2. Dual-mode sensing application of FMNS@Au in buffer

First, latent proMMP-2 was activated by aminophenyl mercuric acetate (APMA) in accordance with the procedures recommended by the manufacturer. Briefly, 150 μg mL^{-1} proMMP-2 was incubated with 1 mmol L^{-1} APMA in TCNB buffer (50 mM Tris, 150 mM NaCl, 10 mM $CaCl_2$ and 0.05% Brij-35; pH 7.5) at 37 °C for 1 h. Next, 10 μL of 5 mg mL^{-1} FMNS@Au solution was incubated with various concentrations of MMP-2 in 350 μL TCNB buffer at 37 °C for 1.5 h. At the end of the incubation, the mixtures were isolated on a magnetic scaffold, and the resulting sediments were resuspended in TCNB buffer. Finally, the fluorescence and SERS spectra of the mixtures were measured at excitation wavelengths of 540 nm and 785 nm (diode laser), respectively. To evaluate its selectivity, the FMNS@Au nanosensors were incubated with a series of molecules and enzymes under optimized conditions.

2.3. Dual-mode detection of MMP-2 activity in cell secretions and human serum samples

The detail procedures for MMP-2 activity determination in cell secretions refer to supporting information. Human serum samples were diluted 10-fold prior to analysis. MMP-2 activity in the diluted serum samples was then measured using the FMNS@Au nanosensor. In addition, known amounts of MMP-2 were added to the diluted serum to prepare spiked samples. The serum samples were then processed as described above for the determination of MMP-2 in buffer, and the fluorescence and SERS signals were then measured.

3. Results and discussion

3.1. Construction and characterizations of the FMNS@Au dual-mode nanosensor

The hybrid FMNS@Au nanosensors were obtained by assembling of FMNS and AuNPs through the highly specific biological recognition between avidin and biotin. In a typical preparation, carboxylated MNS and AuNPs were synthesized according to previous methods (Xie et al., 2005; Qi et al., 2019), and were then characterized by TEM. The TEM images (Supporting Information (SI) Fig. S1) clearly display that the as-synthesized AuNPs, MNS and FMNS@Au were well-dispersed, with mean sizes of 25.3 ± 4.7, 136.2 ± 6.3 and 186.4 ± 10.6 nm in diameters, respectively. As shown in Fig. S2a, an absorption peak characteristic of RB at (λ_{max}, 563 nm) was observed in the FMNS sample, indicating the successful conjugation of RB-avidin with MNS. The strong and broad absorption peak (λ_{max}, 531 nm) observed in FMNS@Au originates from the plasmonic band of the individual AuNPs, demonstrating successful assembly of FMNS and AuNPs (Fig. S2b). The zeta potential of FMNS@Au was −10.3 mV, which was obviously different from that of Au@biotin-pep (3.7 mV, Fig. S3a). This observation provides additional verification for the successful conjugation of AuNPs on the core surface of FMNS. The observed variations in hydrodynamic size (Fig. S3b) are also consistent with the successful preparation of nanosensors.

In addition, the formation of FMNS@Au nanosensors could be observed in TEM images. As demonstrated in Fig. 1a and b, AuNPs were successfully assembled on the surface of FMNS to generate "core-satellite"-shaped architecture. Furthermore, from the HAADF-STEM micrograph and corresponding elemental mapping (Fig. 1d–h), Fe element was observed to be concentrated in the core of the nanohybrids and Au element was densely distributed around the Fe element. The HRTEM micrographs indicate that the d-spacing for adjacent lattice planes were 0.31 nm and 0.24 nm, indexing to the (220) plane of Fe and the (111) plane of Au, respectively (Fig. 1i–ii). The XRD indices of (111), (220), (311), and (511) from FMNS@Au are shown in Fig. 1c. Here the existence of the (111) and (311) peaks provide evidence for the presence of AuNPs on the surface of FMNS. Finally, the XPS measurement results decisively show the presence of Au 4f, Fe 2p and O 1s peaks in FMNS@Au (Fig. 1i–l). Together, the above results provide conclusive confirmation of the successful fabrication of the FMNS@Au nanosensor.

Next, the fluorescence spectra of MNS, RB-avidin, FMNS and FMNS@Au were measured. As shown in Fig. S5, a prominent fluorescence signal was observed for FMNS following RB-avidin modification. In comparison, the fluorescence signal obtained for FMNS@Au was quenched by ca. 80% compared with FMNS. These results demonstrate that FRET occurs between the FMNS and AuNPs with high energy transfer efficiency. In addition, the fluorescence decay curves of FMNS and FMNS@Au at 605 nm were recorded and compared (Fig. S6). The slight reduction in fluorescence lifetime is consistent with the existence of a near-field interaction between FMNS and AuNPs. in FMNS@Au nanosensors. The magnetic hysteresis loops shown in Fig. S7 demonstrate that MNS and FMNS@Au both possess remarkable superparamagnetic properties, with saturation magnetization (Ms) values of 17.73 and 6.96 emu g^{-1} at room temperature, respectively. Thus, FMNS@Au is also amenable to magnetic enrichment and separation. Next, the polydispersity index (PDI) values of the nanosensors in TCNB buffer were obtained from dynamic light scattering (DLS) measurements. In all cases, the PDI values were less than 0.5 (Table S1), indicating moderate dispersity. In addition, the FMNS@Au nanosensors exhibit reasonable stabilities when dispersed in TCNB buffer, 10% DMEM and 10% serum for up to 72 h (Fig. S8). Together, these results demonstrate the practical potential of our novel nanosensor for use in biological analysis.

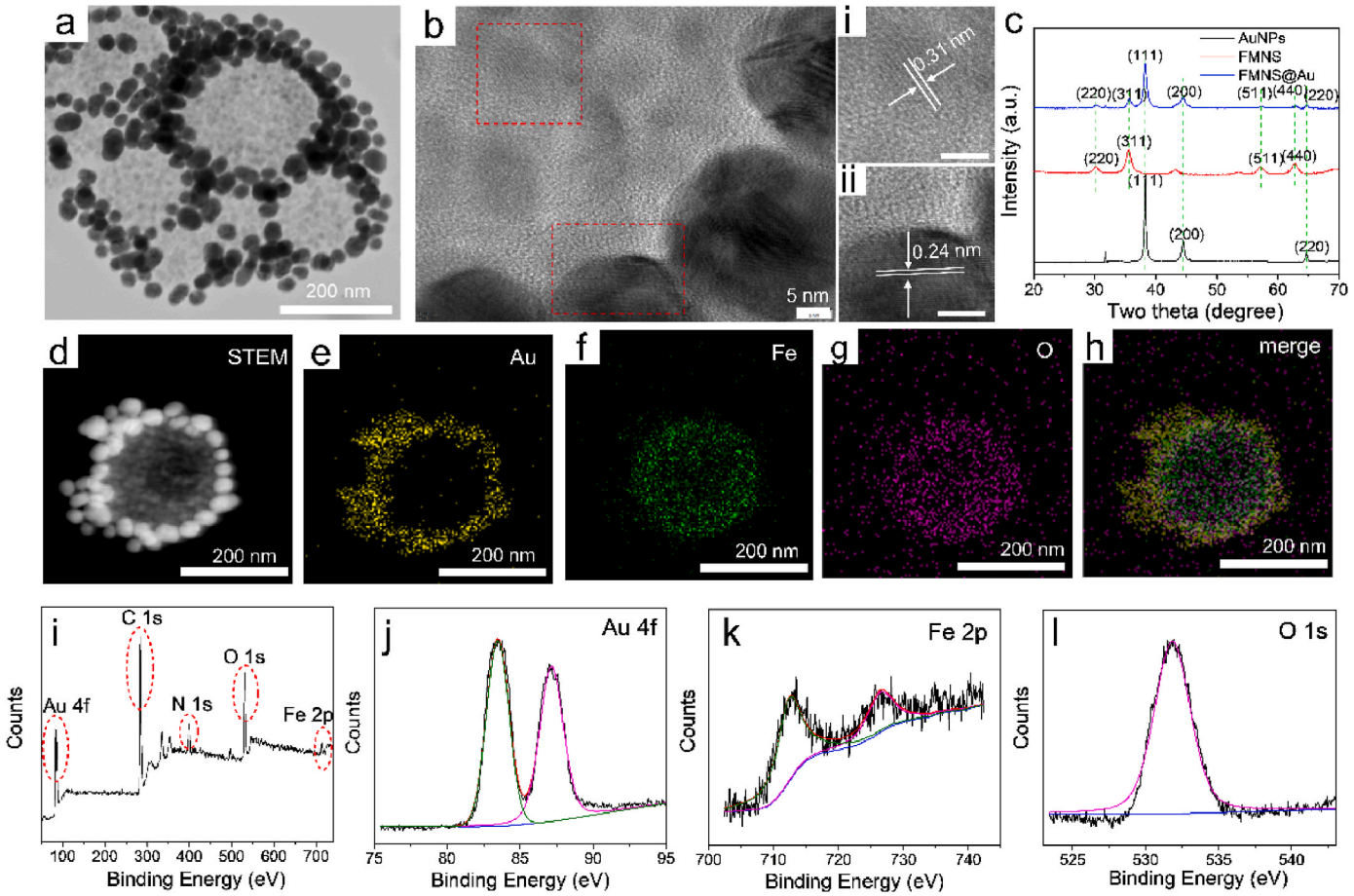

Fig. 1. (a) TEM image of FMNS@Au nanosensors (scale bar, 200 nm). (b) High resolution ratio TEM image of the edge of FMNS@Au (scale bar, 5 nm). (i, ii) The corresponding detail micrographs of the selected regions in (b), representing the Fe_3O_4 NPs embedded in FMNS and AuNPs, respectively. (c) The XRD patterns of Au@biotin-pep, FMNS, and FMNS@Au. (d) HAADF-STEM micrograph of FMNS@Au. (e–h) The elemental mapping of FMNS@Au. (i) The XPS spectra of FMNS@Au nanosensors. (j–l) The detailed peaks of elements Au, Fe, and O in (i), respectively.

3.2. The "hot spots" effect and the effectiveness of FMNS@Au nanosensor for MMP-2 detection

The core-satellite configuration of the FMNS@Au nanosensor contributes to generating "hot spots" that enhance the electromagnetic field to realize SERS signal amplification. The electric field intensity distributions of AuNP, MNS and FMNS@Au are shown in Fig. 2a–c, respectively. These field intensity distributions were generated from finite-difference-time domain (FDTD) simulations, employing parameters (mean diameter and mean gap size) acquired from TEM measurements (Figs. S1 and S9). Individually, AuNP (Fig. 2a) and MNS (Fig. 2b) exhibit relatively weak electromagnetic field enhancement effects. In contrast, FMNS@Au exhibits strong electromagnetic field enhancement (Fig. 2c). This enhancement is a consequence of the architecture of FMNS@Au, which provides favorable conditions for "hot spot" generation and subsequent SERS enhancement. The strong electromagnetic field enhancement provided by "hot spots" was verified by the observably enhanced SERS signal of RB observed at 1647 cm^{-1} (Fig. S10), which can be assigned to aromatic C–C stretching vibration (Table S2). In addition, Fig. S10 shows the SERS spectra of FMNS@Au at each decoration step. The results indicate that there is minimal interference from other substances during the SERS detection of MMP-2.

Subsequently, the efficacy of FMNS@Au nanosensor for determination of MMP-2 was evaluated. As shown in Fig. 2d, the number of AuNPs assembled on FMNS was decreased after incubation with MMP-2, and the core-satellite architecture of FMNS@Au was disassembled. Therefore, the response of FMNS@Au nanosensors towards MMP-2 was as expected. To evaluate the effectiveness of FMNS@Au nanosensors for the identification and detection of MMP-2, the ICP-MS and UV–Vis spectra of FMNS@Au were measured before and after incubation with MMP-2. As shown in Fig. 2e and f, MMP-2 specific cleavage was accompanied by a reduction in Au content and a decrease in the absorbance of FMNS@Au at 531 nm. Together, these results verify the effectiveness of the nanosensor for detecting MMP-2 specific cleavage.

3.3. Sensing performance of the FMNS@Au dual-mode nanosensor in buffer

In order to guarantee the sufficient cleavage of the peptide in the FMNS@Au nanosensor by MMP-2, the kinetic experiment of the reaction between MMP-2 and FMNS@Au was investigated. As shown in Fig. S11, the fluorescence intensity of RB gradually increased with increasing concentration of FMNS@Au and then levelled off when the concentration of FMNS@Au reached 5 mg mL^{-1}. Finally, 5 mg mL^{-1} FMNS@Au was used in the subsequent experiments. To optimize the reaction between FMNS@Au and MMP-2, the influence of incubation time on F_R and I_R was explored. Herein, $F_R = (F - F_0)/F_0$, where F_0 and F represent the maximum fluorescence intensities of FMNS@Au before and after incubation with MMP-2, respectively. In addition, $I_R = (I_0 - I)/I_0$, where I_0 and I represent the SERS signals of FMNS@Au at 1647 cm^{-1} before and after incubation with MMP-2, respectively. The F_R and I_R were both observed to gradually increase with the incubation time, reaching a plateau at approximately 90 min (Fig. 3a and e). Therefore, 90 min was chosen as the optimal incubation time for all the following experiments.

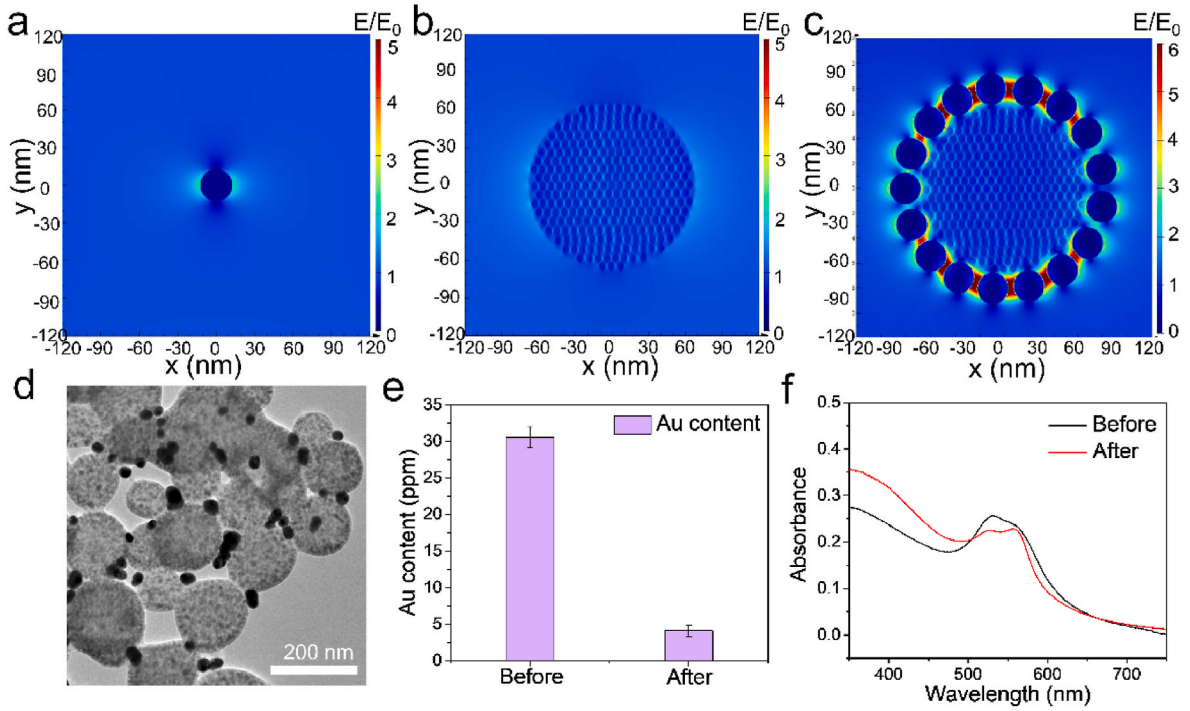

Fig. 2. (a–c) Simulated electric-field intensity distributions of AuNP, MNS and FMNS@Au, respectively, under excitation of 785 nm incident light. (d) TEM image of the FMNS@Au nanosensors after reaction with MMP-2 (200 ng mL^{-1}). (e) The Au content of FMNS@Au nanosensors before and after reaction with MMP-2 (200 ng mL^{-1}). (f) UV–vis spectra of FMNS@Au nanosensors before and after incubation with MMP-2.

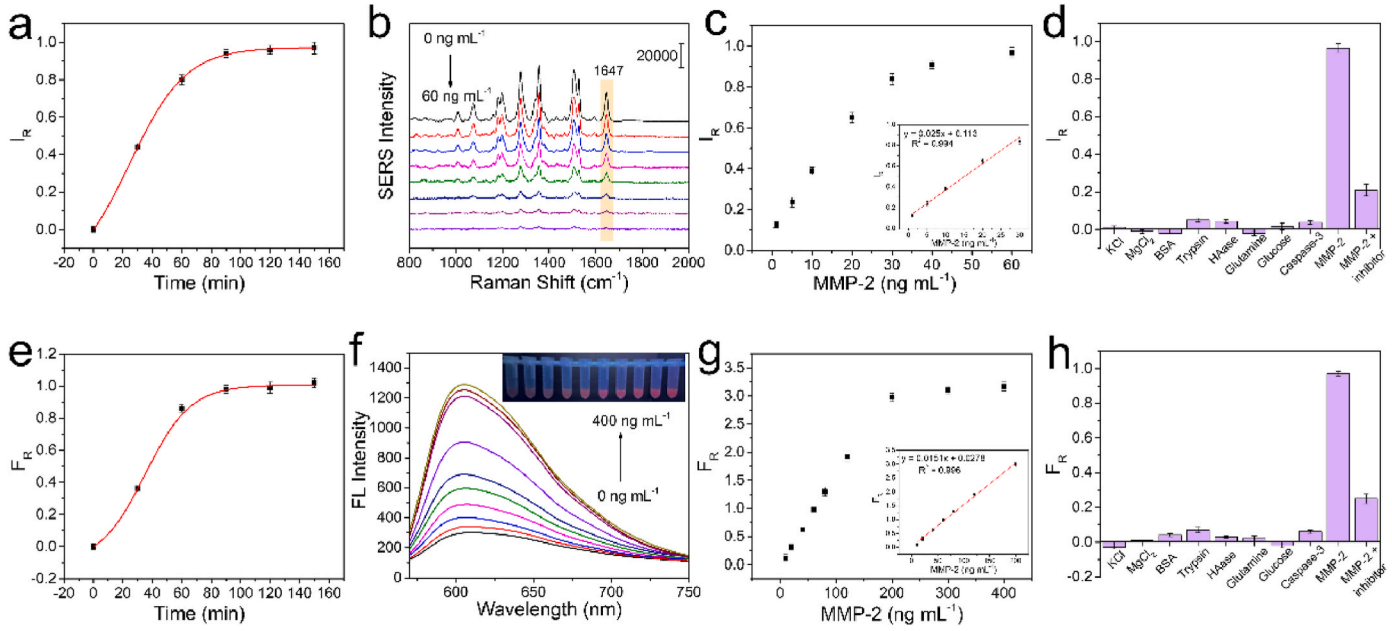

Fig. 3. (a, e) The I_R and F_R of FMNS@Au treated with 60 ng mL^{-1} MMP-2 at various incubation times, respectively. (b, f) SERS and Fluorescence spectra of FMNS@Au treated with various concentrations of MMP-2, respectively. (c, g) Linear relationship of I_R at 1647 cm^{-1} and F_R at 605 nm versus MMP-2 concentration, respectively. (d, h) The I_R and F_R of FMNS@Au in response to potential interfering substances in a selectivity test. The error bars represent standard deviations (n = 3).

As shown in Fig. 3b, the SERS intensity of RB at 1647 cm^{-1} gradually decreased with increasing concentration of MMP-2 in the 0–60 ng mL^{-1} range. A good linear correlation was obtained between I_R and MMP-2 concentration over the 1–30 ng mL^{-1} range, with a limit of detection (LOD) of 0.35 ng mL^{-1} (S/N = 3) and a limit of quantitation (LOQ) of 1.17 ng mL^{-1} (S/N = 10). Conversely, the fluorescence intensity of RB gradually recovered with increasing MMP-2 concentration over the 0–400 ng mL^{-1} range, reaching saturation at 200 ng mL^{-1} (Fig. 3f and g). The increase in fluorescence intensity with MMP-2 concentration over the 0–400 ng mL^{-1} was also imaged under excitation with a 365 nm UV light (inset of Fig. 3f). Thus, MMP-2 activity could be semi-quantitatively analyzed by the naked eye through the nanosensor fluorescence response. A linear relationship between F_R and MMP-2 concentration was observed over the 10–200 ng mL^{-1} range (Fig. 3g), with a

LOD of 2.5 ng mL^{-1} (S/N = 3) and a LOQ of 8.33 ng mL^{-1} (S/N = 10).

As discussed above, the minimum LOD and LOQ for MMP-2 detection employing the dual-mode FMNS@Au nanosensors in buffer were 0.35 ng mL^{-1} and 1.17 ng mL^{-1}, respectively. Importantly, the combination of SERS and fluorescence methods in the FMNS@Au nanosensor broadened the detection range for MMP-2 to 1–200 ng mL^{-1}. Consequently, the developed FMNS@Au nanosensor has good performance for MMP-2 determination as compared with previous methods (Table S3). To examine its selectivity, FMNS@Au was incubated (under optimal conditions) with a range of potential interfering molecules and enzymes, including KCl, $MgCl_2$, trypsin, BSA, HAase, Glutamine, Glucose, caspase-3 and MMP-2 plus inhibitor. FMNS@Au exhibited the strongest response against MMP-2 among other analytes (as shown in Fig. 3d and h and Fig. S12). These results provide evidence that the dual-mode FMNS@Au nanosensor has reasonable selectivity towards MMP-2.

3.4. Determination of MMP-2 activity in cell secretions

To further examine the practicability of the FMNS@Au dual-mode nanosensor, the activity of cell-secreted MMP-2 was determined using the FMNS@Au. To properly assess these measurements of cell-secreted MMP-2 activity, five cell lines including one normal cell (human colon epithelial cell (NCM460)) and four cancer cells (human osteosarcoma cell (MG-63), human colorectal cancer cell (SW480), human breast carcinoma cell (MDA-MB-231) and human lung cancer cell (A549)) were chosen for testing. In all cases, cells were seeded at an identical density of 1×10^5 cells per well. The activities of cell-secreted MMP-2 in conditioned culture medium were then measured using the FMNS@Au nanosensor. As shown in Fig. 4a, the I_R and F_R of FMNS@Au both exhibited obvious differences between the various cell lines (the corresponding fluorescence and SERS spectra are displayed in Fig. S13). In particular, the levels of MMP-2 secreted by tumor cell lines were higher than that secreted by the normal cell line (NCM460). Moreover, the activities of MMP-2 secreted by MDA-MB-231 and MG-63 were higher than those secreted by A549 and SW480. These results indicate that MMP-2 activity is correlated with the pathological characteristics of tumor cell lines, particularly the degree of tumor malignancy (Roomi et al., 2009; Sakata et al., 2000; Bauvois, 2012). The corresponding fluorescence images acquired under a 365 nm UV light clearly demonstrate the differences in the levels of MMP-2 secreted by cancer cells and normal cells (Fig. S14). Thus, it is possible to distinguish between normal cells and cancer cells by the naked eye observation. The quantification results obtained using the FMNS@Au nanosensor were also compared with the commercial MMP-2 ELISA kit (Table S4). The calibration curve for the MMP-2 ELISA kit is shown in Fig. S17. The results produced using the FMNS@Au were in accordance with those obtained using the MMP-2 ELISA kit, demonstrating the good reliability of the FMNS@Au dual-mode nanosensor.

To assess the influence of cell density on MMP-2 activity measurements, MG-63 cells were employed because they exhibit high MMP-2 secretion levels and high metastatic characteristics (Kempf--Bielack et al., 2005; Kager et al., 2003). As shown in Fig. 4b, the MMP-2 secretion levels of MG-63 cells reached a maximum at 1×10^5 cells per well, and then decreased by increasing/decreasing cell seeding densities. The result demonstrates that high cell densities can inhibit MMP-2 activity levels in MG-63 cell secretions. The corresponding quantification results are illustrated in Table S5, and the corresponding fluorescence and SERS spectra are displayed in Fig. S15. Again, these results were consistent with those provided by the MMP-2 ELISA kit.

As a specific activator of the ERK pathway, PMA is applied to stimulate the secretion of MMP-2 by MG-63 cells (Ling et al., 2010). As shown in Fig. 4c, the I_R and F_R of FMNS@Au both increased with increasing PMA concentration in the cell culture medium (the corresponding fluorescence and SERS spectra are displayed in Fig. S16). Thus, the results obtained by our novel nanosensor are consistent with published data, demonstrating that MG-63 cells secrete high levels of MMP-2 after PMA stimulation. The full quantification results are given in Table S6. The results obtained using FMNS@Au are also in good agreement with those obtained using the MMP-2 ELISA kit. Together, these results confirm that the FMNS@Au dual-mode nanosensor can be effectively used to study MMP-2-related life process.

3.5. Determination of MMP-2 activity in human serum using the FMNS@Au nanosensor

To further assess the applicability of the FMNS@Au dual-mode nanosensor in actual MMP-2-related processes, FMNS@Au was used to determine MMP-2 activity in human serum. First, serum samples from six healthy volunteers were diluted 10-fold to guarantee that MMP-2 concentrations were within the defined linear measurement range. After taking this dilution into account, MMP-2 levels in human serum samples were between 113 and 159 ng mL^{-1} (Table 1), which is in accordance with previous reports of MMP-2 levels in healthy individuals (Colotti et al., 2007). Standard addition experiments were conducted to further verify the applicability of the FMNS@Au nanosensor. The results presented in Table 1 indicate that the proposed FMNS@Au nanosensor exhibits a recovery efficiency in the range of 89.4–104.1% in serum samples, with RSDs in the range of 2.5–6.8%. Together, these results demonstrate the high practicability and accuracy of the designed nanosensor when assaying MMP-2 activity in human serum.

4. Conclusion

In summary, a multifunctional and bio-self-assembly nanosensor of FMNS@Au has been developed for dual-mode determination of MMP-2 activity levels. In this work, the designed core-satellite FMNS@Au nanosensor provides high density “hot spots” that improve the sensitivity of MMP-2 detection in SERS mode. In addition, a highly efficient

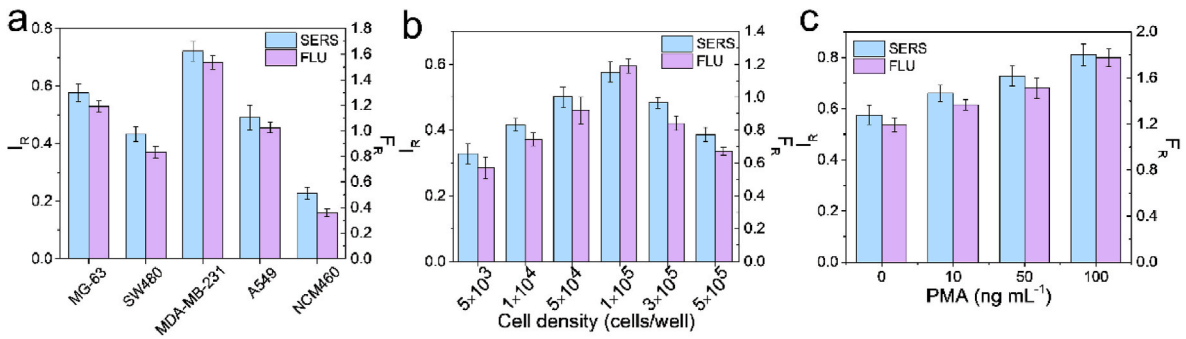

Fig. 4. (a) Data analysis of cell-secreted MMP-2 activity in MG-63, SW480, MDA-MB-231, A549, and NCM460 cell conditioned culture media obtained using FMNS@Au dual-mode nanosensors. Data analysis of the effects of cell density (b) and PMA stimulation (c) on the secretion of MMP-2 from MG-63 cells using FMNS@Au dual-mode nanosensors.

Table 1
Recovery test of MMP-2 in human serum samples using the dual-mode FMNS@Au nanosensors (n = 3).

Sample	Added (ng mL^{-1})	SERS				Fluorescence			
		Initial (ng mL^{-1})	Found (ng mL^{-1})	Recovery (%)	RSD (%)	Initial (ng mL^{-1})	Found (ng mL^{-1})	Recovery (%)	RSD (%)
1	10	12.3	21.5	92.0	2.9	12.1	21.8	96.7	2.5
2	10	11.3	21.0	97.0	5.1	11.5	20.6	91.0	3.6
3	10	14.1	24.5	104.1	4.2	13.8	24.0	102.1	4.1
4	10	12.6	21.9	93.2	6.8	13.1	22.5	94.2	4.7
5	10	12.4	22.7	102.5	2.6	12.5	22.4	99.8	3.8
6	10	15.3	25.1	98.6	4.7	15.9	24.8	89.4	4.9

FRET system generated within FMNS@Au can be applied to detect MMP-2 in fluorescence mode. The SERS and fluorescence assays in this FMNS@Au nanosensor are complementary and can be tested simultaneously, providing a mutual check system. Importantly, the designed nanosensor affords semi-quantitative sensing of MMP-2 by naked-eye observation and accurate detection of MMP-2 by dual-mode analysis. Moreover, the practicability of the proposed nanosensor was verified by the quantitative measurement of MMP-2 in cell secretions and human serum samples. The dual-mode FMNS@Au nanosensor is a promising tool that can be employed in the clinical diagnosis of various MMP-2 associated diseases. And the sensing strategy is constructive for developing other protease sensors for cancer diagnosis studies.

CRediT authorship contribution statement

Lin Liu: Conceptualization, Methodology, Software, Investigation, Data curation, Writing – original draft. **Hongyu Chu:** Formal analysis, Validation. **Jukun Yang:** Investigation, Software. **Ying Sun:** Data curation, Validation. **Pinyi Ma:** Conceptualization, Project administration, Data curation, Writing – review & editing. **Daqian Song:** Project administration, Funding acquisition, Resources, Supervision.

Declaration of competing interest

The authors declare that they have no known competing financial interests or personal relationships that could have appeared to influence the work reported in this paper.

Acknowledgement

The authors would like to thank the National Natural Science Foundation of China (Grant Nos. 22074052 and 22004046) for financial support.

Appendix A. Supplementary data

Supplementary data to this article can be found online at https://doi.org/10.1016/j.bios.2022.114389.

References

Bauvois, B., 2012. Biochim. Biophys. Acta 1825, 29–36.
Cao, Y., Qian, R.C., Li, D.W., Long, Y.T., 2015. Chem. Commun. 51, 17584–17587.
Cheng, H., Li, S.Y., Zheng, H.R., Li, C.X., Xie, B.R., Chen, K.W., Li, B., Zhang, X.Z., 2017. Anal. Chem. 89, 4349–4354.
Colotti, C., Angeli, V., Del Ry, S., Maltinti, M., Vittorini, S., Giannessi, D., 2007. Clin. Chem. Lab. Med. 45, 1292–1298.
Davies, B., Waxman, J., Wasan, H., Abel, P., Williams, G., Krausz, T., Neal, D., Thomas, D., Hanby, A., Balkwill, F., 1993. Cancer Res. 53, 5365–5369.
Fang, J.M., Shing, Y., Wiederschain, D., Yan, L., Butterfield, C., Jackson, G., Harper, J., Tamvakopoulos, G., Moses, M.A., 2000. Proc. Natl. Acad. Sci. Unit. States Am. 97, 3884–3889.
Farka, Z., Juriik, T., Kovaar, D., Trnkova, L., Sklaadal, P., 2017. Chem. Rev. 117, 9973–10042.
Gao, X.T., Ma, G.C., Jiang, C., Zeng, L.L., Jiang, S.S., Huang, P., Lin, J., 2019. Anal. Chem. 91, 7112–7117.
Gong, T.X., Hong, Z.Y., Chen, C.H., Tsai, C.Y., Liao, L.D., Kong, K.V., 2017. ACS Nano 11, 3365–3375.
Huang, Y., Qi, Y., Zhan, C.Y., Zeng, F., Wu, S.Z., 2019. Anal. Chem. 91, 8085–8092.
Kager, L., Zoubek, A., Potschger, U., Kastner, U., Flege, S., Kempf-Bielack, B., Branscheid, D., Kotz, R., Salzer-Kuntschik, M., Winkelmann, W., Jundt, G., Kabisch, H., Reichardt, P., Jurgens, H., Gadner, H., Bielack, S.S., 2003. Cooperat German-Austrian-Swiss, O. J. Clin. Oncol. 21, 2011–2018.
Kempf-Bielack, B., Bielack, S.S., Jurgens, H., Branscheid, D., Berdel, W.E., Exner, G.U., Gobel, U., Helmke, K., Jundt, G., Kabisch, H., Kevric, M., Klingebiel, T., Kotz, R., Maas, R., Schwarz, R., Semik, M., Treuner, J., Zoubek, A., Winkler, K., 2005. J. Clin. Oncol. 23, 559–568.
Kessenbrock, K., Plaks, V., Werb, Z., 2010. Cell 141, 52–67.
Krpetic, Z., Guerrini, L., Larmour, I.A., Reglinski, J., Faulds, K., Graham, D., 2012. Small 8, 707–714.
Lei, Z., Jian, M.H., Li, X.T., Wei, J., Meng, X.Y., Wang, Z.X., 2020. J. Mater. Chem. B 8, 3261–3291.
Li, C.C., Hu, J., Luo, X., Hu, J., Zhang, C.Y., 2021. Anal. Chem. 93, 14568–14576.
Li, D., Ma, Y.D., Duan, H.Z., Jiang, F., Deng, W., Ren, X.G., 2018. Anal. Chim. Acta 1038, 148–156.
Li, X., Deng, D.W., Xue, J.P., Qu, L.Z., Achilefu, S., Gu, Y.Q., 2014. Biosens. Bioelectron. 61, 512–518.
Li, Y.Y., Liu, W., Xu, Q.F., Hu, J., Zhang, C.Y., 2020. Biosens. Bioelectron. 169, 112647.
Lin, D., Hsieh, C.L., Hsu, K.C., Liao, P.H., Qiu, S.F., Gong, T.X., Yong, K.T., Feng, S.Y., Kong, K.V., 2021. Nat. Commun. 12, 3430.
Ling, H., Yang, H., Tan, S.H., Chui, W.K., Chew, E.H., 2010. Br. J. Pharmacol. 161, 1763–1777.
Liu, Y.H., Duan, W.X., Song, W., Liu, J.J., Ren, C.L., Wu, J., Liu, D., Chen, H.L., 2017. ACS Appl. Mater. Interfaces 9, 12663–12672.
Puperi, D.S., O'Connell, R.W., Punske, Z.E., Wu, Y., West, J.L., Grande-Allen, K.J., 2016. Biomacromolecules 17, 1766–1775.
Qi, G.H., Li, H.J., Zhang, Y., Li, C.P., Xu, S.P., Wang, M.M., Jin, Y.D., 2019. Anal. Chem. 91, 1408–1415.
Quintero-Fabian, S., Arreola, R., Becerril-Villanueva, E., Torres-Romero, J.C., Arana-Argaez, V., Lara-Riegos, J., Ramirez-Camacho, M.A., Alvarez-Sanchez, M.E., 2019. Front. Oncol. 9, 1370.
Roomi, M.W., Monterrey, J.C., Kalinovsky, T., Rath, M., Niedzwiecki, A., 2009. Oncol. Rep. 21, 1323–1333.
Sakata, K., Shigemasa, K., Nagai, N., Ohama, K., 2000. Int. J. Oncol. 17, 673–681.
Sheen-Chen, S.-M., Chen, H.-S., Eng, H.-L., Sheen, C.-C., Chen, W.-J., 2001. Cancer Lett. 173, 79–82.
Stearns, M.E., Wang, M., 1993. Cancer Res. 53, 878–883.
Sun, C., Dong, W., Peng, J., Wan, X., Sun, Z., Li, D., Wang, S., 2020. Sensor. Actuator. B Chem. 325, 128644.
Wang, C.W., Li, P., Wang, J.F., Rong, Z., Pang, Y.F., Xu, J.W., Dong, P.T., Xiao, R., Wang, S.Q., 2015. Nanoscale 7, 18694–18707.
Wang, Y.H., Shen, P., Li, C.Y., Wang, Y.Y., Liu, Z.H., 2012. Anal. Chem. 84, 1466–1473.
Xi, X.X., Wen, M.Q., Song, S.H., Zhu, J.L., Wen, W., Zhang, X.H., Wang, S.F., 2020. Chem. Commun. 56, 6039–6042.
Xie, H.Y., Zuo, C., Liu, Y., Zhang, Z.L., Pang, D.W., Li, X.L., Gong, J.P., Dickinson, C., Zhou, W.Z., 2005. Small 1, 506–509.
Yan, R.Q., Hu, Y.X., Liu, F., Wei, S.X., Fang, D.Q., Shuhendler, A.J., Liu, H., Chen, H.Y., Ye, D.J., 2019. J. Am. Chem. Soc. 141, 10331–10341.
Yang, G., Li, L., Rana, R.K., Zhu, J.J., 2013. Carbon 61, 357–366.
Yang, T.X., Guo, X.Y., Wang, H., Fu, S.Y., Wen, Y., Yang, H.F., 2015. Biosens. Bioelectron. 68, 350–357.
Zhang, J., Ma, X., Wang, Z., 2019. Anal. Chem. 91, 6600–6607.
Zhang, Q., Wu, Y., Xu, Q., Ma, F., Zhang, C.Y., 2021. Biosens. Bioelectron. 171, 112712.